Tunable intrinsic spin Hall conductivity in bilayer $PtTe_2$ by controlling the stacking mode

Jianwei Li, Hao Jin,* and Yadong Wei
College of Physics and Optoelectronic Engineering, Shenzhen University, Shenzhen 518060, China

Hong Guo
College of Physics and Optoelectronic Engineering, Shenzhen University, Shenzhen 518060, China
and Centre for the Physics of Materials and Department of Physics, McGill University, Montreal, Quebec, Canada H3A 2T8

(Received 29 November 2020; revised 8 February 2021; accepted 22 February 2021; published 3 March 2021)

We report a systematic study on the intrinsic spin Hall conductivity (ISHC) of bilayer $PtTe_2$ and explore the connection between the stacking order and ISHC. We find that by changing the stacking mode, ISHC can be manipulated from positive to negative values. Such strong stacking-dependent ISHC originates from the interlayer coupling, in which Te atoms in the upper and lower layers can form either van der Waals or covalentlike quasibonding depending on the stacking modes. Thus ISHC can be effectively tuned by changing the stacking order. These results not only allow us to establish fundamental understanding of ISHC in bilayer $PtTe_2$ dependent on the stacking mode but also provide guidelines for the application of bilayer $PtTe_2$ in next-generation spintronic devices.

DOI: 10.1103/PhysRevB.103.125403

I. INTRODUCTION

Spintronics is considered as a promising solution to overcome the Joule heating generated in electronic devices, in which the electronic and spin degrees of freedom of carriers are utilized to control the properties of materials and devices. In the field of spintronics, spin current is one of the key physical quantities. Generation and manipulation of spin currents are of fundamental and technical significance for spintronic devices. Among all possible approaches, the spin Hall effect (SHE), which provides an efficient way to convert charge current into spin current without magnetic field, attracts much attention [1–5]. The SHE has a close relationship to the anomalous Hall effect (AHE), which was proposed by Dyakonov and Perel based on the assumption of extrinsic electron scattering [6,7]. Since then, a number of studies have been devoted to exploring the mechanism behind the SHE [3,8–11]. In general, the SHE originates from three distinct mechanisms, i.e., the skew scattering, the side jump, and the intrinsic mechanisms. The first two mechanisms are also known as the extrinsic SHE and are due to impurity scattering and therefore sensitive to the character of the impurity potential [12–16]. By contrast, the intrinsic SHE is independent of the presence of impurities and depends only on details of the electronic band structure of the perfect crystal [1,3,5].

The intrinsic effect, which may dominate the total SHE in those materials with strongly spin-orbit-coupled bands, has a direct link with the semiclassical theory in which the induced interband coherence is captured by an anomalous velocity due to the Berry curvature in momentum space [5]. This intrinsic contribution was developed by Jungwirth *et al*. for AHE in ferromagnetic semiconductors [17] and then extended to SHE by Murakami *et al*. [1] in a p-type semiconductor and Sinova *et al*. [3] in a two-dimensional (2D) electron system with substantial Rashba spin-orbit coupling. Motivated by these results, a number of studies have been done to predict the intrinsic spin Hall conductivity (ISHC), especially for metals. For example, using density functional theory (DFT), Guo *et al*. found that the ISHC could be as large as $\sim 2000\ (\hbar/e)\,(\mathrm{S/cm})$ at low temperature [11]. Tanaka *et al*. [18] investigated $4d$ and $5d$ metals based on the tight-binding model and showed that the sign of the ISHC could be changed from Nb to Ag (Ta to Au) for $4d$ ($5d$) metals, which was later observed in experiments [19]. A strong anisotropy of ISHC was also reported by Freimuth *et al*. in nonmagnetic hcp metals and antiferromagnetic Cr [20]. In addition, the ISHC can be further enhanced by substitutional doping, which can be ascribed to the synergistic behavior of ISHC and longitudinal conductivity with the Fermi level position [21].

It should be mentioned that most of the previous studies focus on heavy metals (e.g., Pt, W, and Ta). Though their ISHC is large, it is considerably difficult to control and manipulate the spin current in this kind of material. Thus searching for novel materials with tunable ISHC becomes highly desirable. The discovery of 2D layered material has offered an opportunity to create and control spin current through SHE [22,23]. As an attractive class of 2D layered materials, transition metal dichalcogenides (TMDs) are appealing because of their rich physics and potential applications [24–27]. However, theoretical studies related to intrinsic SHE in 2D materials are limited to a few works which focused only on monolayer structures [28–30]. It is worthwhile to mention that the bilayer or multilayer stacks can exhibit more intriguing properties. Furthermore, by changing the stacking order between

*jh@szu.edu.cn

different layers, the electronic structures and physical properties can be effectively tuned, which may be apparently different from the bulk or monolayer counterparts. For example, the out-of-plane ferroelectric polarization of bilayer VS_2 was predicted to be reversed upon interlayer sliding [31]. Recently, Xiao *et al*. also demonstrated a nonvolatile memory based on Berry curvature through electrically driven stacking transition in few-layer WTe_2 [32]. Nevertheless, the connection between the stacking order and the intrinsic SHE in 2D materials yet remains unclear. In this sense, a comprehensive understanding of the intrinsic SHE manipulated by stacking order in 2D materials is necessary. On the other hand, compared with group-6 TMDs (e.g., MoS_2), group-10 TMDs show strong interlayer coupling, which may be sensitive to the stacking order and can dramatically affect the electronic properties and band structures [33,34]. In addition, it is reported that 2D $PtTe_2$ remains metallic even down to bilayer thickness, which exhibits to date the highest electrical conductivity at room temperature and the largest ISHC among all investigated metallic TMDs [26,34–36]. In view of the fact that the intrinsic SHE is dependent on the band structure of the material, bilayer $PtTe_2$ may provide a promising platform to explore the influence of stacking order on the intrinsic SHE, which calls for further investigation.

In this paper, we take $PtTe_2$ as an example and explore the connection between the intrinsic SHE and the stacking order. Here, based on the DFT study, we find that the strength of interlayer interaction is different depending on the stacking orders. For the AB′ stacking mode, the interlayer coupling is weak with a relatively long interlayer distance, suggesting a van der Waals (vdW) characteristic. In this case, there exists a tiny energy gap, and the bilayer $PtTe_2$ shares a similar behavior of ISHC with its single-layer counterpart. When the system slides to AB stacking mode, a medium interlayer interaction is observed with a small number of electrons appearing in the interlayer region. The enhanced interlayer coupling lifts the valence bands upwards that cross the Fermi level, leading to the transition from semiconductor to metal. As a result, a positive ISHC is observed at the Fermi level. For the AA stacking mode, the interlayer coupling between the top and bottom layers becomes so strong that they form covalentlike quasibonding. In addition, a large number of electrons are observed to localize within the interlayer region. Electronic bands are significantly modified, which reverses their contributions to the spin Berry curvature, thus resulting in the reversion of ISHC from positive to negative values. Through this study, we analyze the mechanism for intrinsic SHE by spin Berry curvature and illustrate that the interlayer stacking order is an efficient way to control and manipulate the ISHC dynamically in bilayer TMDs.

The rest of the paper is organized as follows. In Sec. II, the DFT setup and theoretical details of calculating the ISHC are presented. The electronic properties and results of the ISHC for a $PtTe_2$ bilayer with different stacking configurations are discussed in Sec. III. Finally, a brief conclusion is given in Sec. IV.

II. COMPUTATIONAL METHODOLOGY

Our DFT calculations are performed using the QUANTUM ESPRESSO package [37,38], in which the projector augmented-wave method and a plane-wave basis set are employed. The exchange-correlation interactions are treated by generalized gradient approximation of the Perdew-Burke-Ernzerhof approach [39]. The plane-wave cutoff is chosen to be 90 Ry, and the first Brillouin zone is sampled using a Γ-centered k mesh with 12×12, which gives rise to good convergence. To better describe the vdW interaction, the structure is relaxed using the DFT-D3 vdW corrections [40]. A vacuum of 20 Å is used to avoid the interactions between adjacent slabs. In this paper, we use maximally localized Wannier functions and the Kubo formula to calculate the ISHC [41–43]. To deal with the rapid variation of the spin Berry curvature, the Brillouin zone integration is carried out using a dense k mesh with 300×300.

The Kubo formula for ISHC is given by [43,44]

$$\sigma_{xy}^{z} = \frac{e}{\hbar}\int_{\mathrm{BZ}} \frac{d\mathbf{k}}{(2\pi)^2}\Omega_{xy}^{z}(\mathbf{k}). \tag{1}$$

$\Omega_{xy}^{z}(\mathbf{k})$ is the $\mathbf{k}$-resolved term, which is given by

$$\Omega_{xy}^{z}(\mathbf{k}) = \sum_{n} f_{kn}\Omega_{n,xy}^{z}(\mathbf{k}), \tag{2}$$

where f_{kn} is the Fermi-Dirac distribution function and $\Omega_{n,xy}^{z}(\mathbf{k})$ is the band-projected spin Berry curvature given as

$$\Omega_{n,xy}^{z}(\mathbf{k}) = -\sum_{n'\neq n} \frac{2Im[\langle \mathbf{k}n|\hat{j}_x^z|\mathbf{k}n'\rangle\langle \mathbf{k}n'|\hat{v}_y|\mathbf{k}n\rangle]}{(\epsilon_{\mathbf{k}n} - \epsilon_{\mathbf{k}n'})^2}, \tag{3}$$

where $j_x^z = \frac{1}{2}\{s^z, v_x\}$ is the spin current operator, $s^z = \frac{\hbar}{2}\sigma^z$ is the spin operator, $\hat{v}_y = \frac{1}{\hbar}\frac{\partial H(\mathbf{k})}{\partial k_y}$ is the velocity operator, and $|\mathbf{k}n\rangle$ is the wave function of energy $\epsilon_{\mathbf{k}n}$. σ_{xy}^{z} represents the conductivity of spin current (J_s) generated along the xth direction with spin polarization along z due to an applied electric field along the y direction. Note that in principle, the commonly used spin current operator J_x^z does not satisfy the continuity equation in systems with nonconserved spin. To overcome this issue, Niu and co-workers proposed a new spin current operator based on the semiclassical theory, in which J^z is defined as $J^z = i[H_0, S^z]$ [45,46]. Nonetheless, Monaco and Ulčakar have proved recently that the spin conductivity tensor σ_{xy}^{z} is independent of the choice of spin current operator if the system has mirror symmetry $(x, y) \mapsto (-x, y)$ [47], which is the case in our work, e.g., AA, AB, and AB′ stacking orders. In addition, previous work also reported spin transport properties in Bi_2Se_3 with strong spin-orbit coupling, where tilting of spin is found to be extremely small from a z direction [48]. Therefore the results obtained using our spin current operator should not change if other definitions of the operator are used. So we choose the conventional definition for the spin current operator. Moreover, we should also point out that the calculated spin Berry curvature varies rapidly (see Fig. S1 in the Supplemental Material [49]). As such, when we plot the spin Berry curvature, we take the logarithm of Eqs. (2) and (3), which can make the rapid variation of spin Berry curvature clearer visually. This strategy was also applied in previous

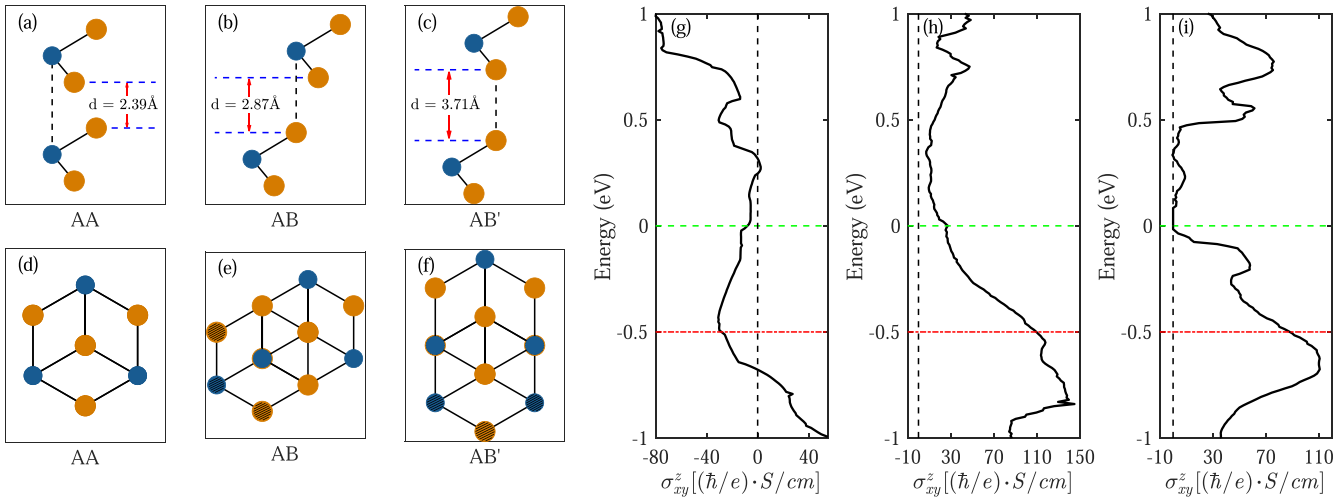

FIG. 1. (a)–(c) Side and (d)–(f) top views of bilayer $PtTe_2$ for AA, AB, and AB′ stacking configurations. Blue and orange circles indicate Pt and Te atoms, respectively. The dashed circles represent atoms in the bottom layer. The ISHC as a function of the Fermi energy for (g) AA, (h) AB, and (i) AB′ stacking configurations. Green and red dashed lines indicate the Fermi levels $E - E_f = 0$ and $E - E_f = -0.5$ eV, respectively. The dashed black line represents the zero value of ISHC.

studies and is defined as [43,50]

$$\Omega' = \begin{cases} \mathrm{sgn}(\Omega)\log_{10}|\Omega| & |\Omega| > 10 \\ \frac{\Omega}{10} & |\Omega| \leqslant 10. \end{cases} \tag{4}$$

Here, sgn(Ω) means taking the sign of Ω.

III. RESULTS AND DISCUSSION

Different from group-6 TMDs, which usually form hexagonal (2H) structures, $PtTe_2$ exhibits trigonal (1T) structure with space group $P\bar{3}m1$, where one Pt atom and the nearest six Te atoms compose a distorted octahedron. When considering the stacking modes in the bilayer, it is necessary to consider three highly symmetric stacking configurations as shown in Fig. 1 and in Fig. S2 in the Supplemental Material [49]. Note that the AA stacking mode corresponds to its bulk stacking order. The optimized lattice constant a and interlayer distance d for AA stacking are $a = 4.01$ Å and $d = 2.39$ Å, respectively (see Table I). These values are very close to its bulk lattice parameters (i.e., $a = 4.01$ Å and $d = 2.62$ Å). Compared with the AA stacking mode, the other stacking configurations have a lateral shift for the top layer. The lattice constants for different stacking orders are basically the same, while the interlayer distance varies from 2.39 Å for AA to 3.71 Å for AB′ stacking orders.

In Figs. 1(g)–1(i), we plot ISHC as a function of the Fermi level for bilayer $PtTe_2$. As shown clearly, AB stacking exhibits the largest ISHC with a value up to 27.18 $(\hbar/e)$(S/cm) at the Fermi level position (i.e., $E - E_F = 0$ eV). When the stacking order is changed, the ISHC varies from positive to negative values. Especially, ISHC for AA stacking is −8.41 $(\hbar/e)$(S/cm). In addition, the trends of ISHC as a function of the Fermi level for each stacking mode are also quite different. For AA stacking, the magnitude of ISHC increases considerably as the Fermi energy is lowered, and peaks at $E - E_F = -0.5$ eV. Further lowering the Fermi energy could reverse the sign of the ISHC. Nevertheless, the ISHC in AA stacking exhibits a negative value over a broad energy range. By contrast, other stacking modes show positive ISHC and have peaks around −0.75 eV. The maximum value of ISHC reaches 142.13 $(\hbar/e)$(S/cm) at $E - E_F = -0.75$ eV for AB stacking.

TABLE I. Calculated lattice constant a, interlayer distance d, binding energy ΔE, and ISHC at Fermi level σ^z_{xy}.

Stacking	a (Å)	d (Å)	ΔE (eV)	σ^z_{xy} $[(\hbar/e)$(S/cm)]
AA	4.01	2.39	−2.691	−8.41
AB	3.97	2.87	−2.481	27.18
AB′	3.98	3.71	−2.298	0

To elucidate the underlying mechanism of ISHC variation induced by stacking modes, we take AA and AB stacking as examples and plot band structures projected by spin Berry curvature $\Omega^z_{n,xy}(\mathbf{k})$ in Fig. 2. The red and blue colors indicate positive and negative contributions, respectively, which are taken from the logarithm of Eq. (3) [defined by Eq. (4)]. Note that the spin-orbit coupling is also included. Since ISHC is mainly contributed by occupied bands near the Fermi level, here we focus on six valence bands that are close to the Fermi energy and denote them as VB1–VB6, labeled in Fig. 2(a). We find that in both stacking modes, VB2–VB5 are mainly composed of Te p_x and p_y orbitals around the Γ point, while VB1 and VB6 originate from the out-of-plane p_z state of Te atoms (see Figs. S3– S6 in the Supplemental Material [49]). At the Fermi level, the ISHC in the AA stacking order exhibits a negative value, which can be ascribed to the contributions by VB2–VB5 around the Γ point. Especially, a deep valley is observed near the Γ point along the $K-\Gamma$ path {see Fig. S7(a) in the Supplemental Material [49]}. By contrast, the ISHC shows a positive value in the AB stacking configuration. This can be understood based on the fact that contributions by VB2–VB5 to the spin Berry curvature reverse their signs along the $K-\Gamma-M$ path, especially for VB4 and VB5. As a result, negative spin Berry curvature weakens, while positive

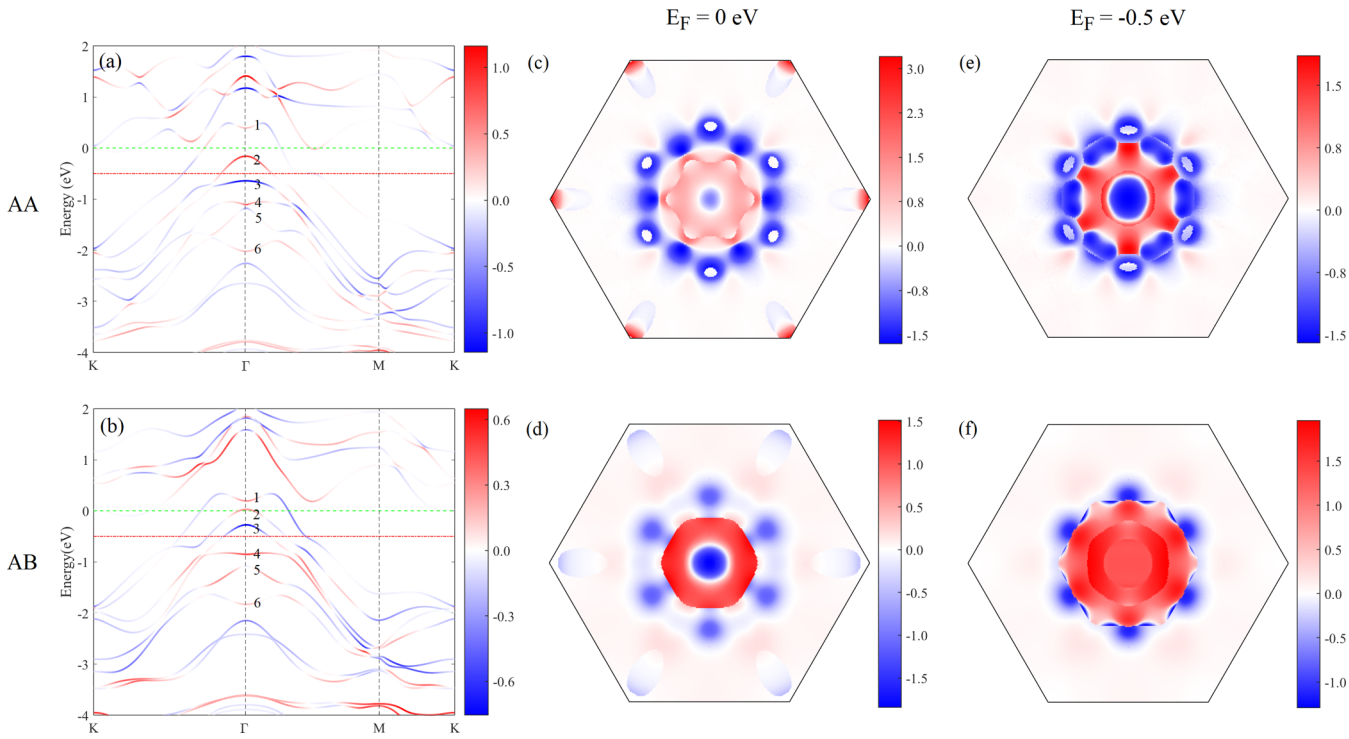

FIG. 2. Band structures projected by taking the logarithm of spin Berry curvature for (a) AA and (b) AB stacking configurations. Green and red dashed lines indicate the energy levels at $E - E_F = 0$ eV and $E - E_F = -0.5$ eV, respectively. k-resolved spin Berry curvature after taking the logarithm of Eq. (2) [defined by Eq. (4)] in the 2D Brillouin zone ($k_z = 0$) at the energy level position of (c) and (d) $E - E_f = 0$ eV and (e) and (f) $E - E_f = -0.5$ eV for AA and AB stacking configurations. Red and blue colors represent positive and negative contributions, respectively.

spin Berry curvature strengthens {see Fig. S7(b) in the Supplemental Material [49]}, resulting in positive ISHC with a value of 27.18 $(\hbar/e)$ (S/cm).

In Figs. 2(c) and 2(d), we show the k-resolved spin Berry curvature $[\Omega^z_{xy}(\mathbf{k})]$ in the 2D Brillouin zone ($k_z = 0$) at the energy positions of $E - E_F = 0$ eV and $E - E_F = -0.5$ eV,

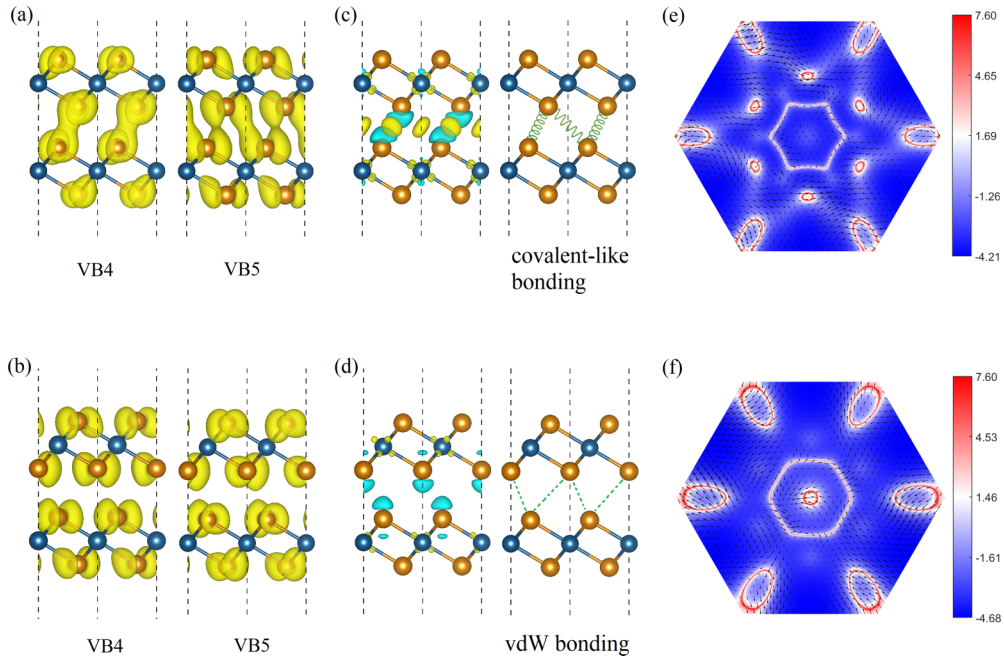

FIG. 3. Band-decomposed charge densities for (a) AA and (b) AB stacking configurations. Interlayer differential charge densities and the simplified models for (c) AA and (d) AB stacking configurations. The light blue and yellow isosurfaces indicate charge depletion and accumulation, respectively. Spin textures for (e) AA and (f) AB stacking configurations.

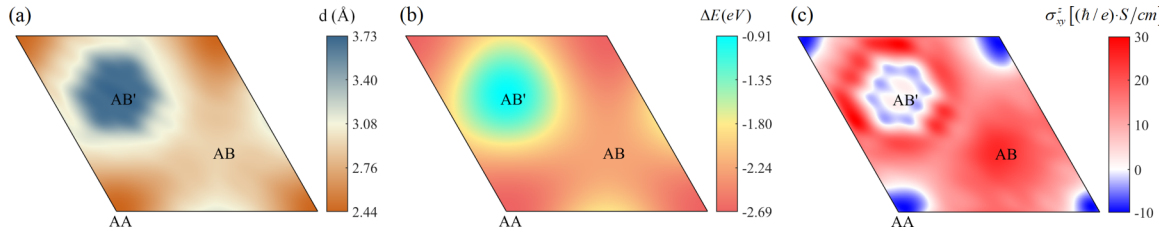

FIG. 4. (a) Interlayer distance, (b) binding energy, and (c) ISHC for the full space of lateral shifts.

respectively. The spin Berry curvature is also colored red (positive contribution) and blue (negative contribution). As has been mentioned above, these values are taken from the logarithm of Eq. (2), i.e., Eq. (4). It can be seen that the spin Berry curvature depends sensitively on the k point. At $k = 0.36$ of the Brillouin zone, a large magnitude of the spin Berry curvature is observed for AA stacking. When k moves away from the Γ point, the spin Berry curvature is close to zero. For AB stacking, however, the spin Berry curvature exhibits a positive value in the range of $0.13 < k < 0.31$, as shown by the red color. It is interesting to note that when the energy is shifted by -0.5 eV, such trends become more remarkable. In the AB stacking order, the positive region expands widely and overwhelms the negative one, especially at the Γ point, giving rise to high ISHC with a value up to 110.68 $(\hbar/e)$ (S/cm). For the AA stacking order, we find significant enhancement of the negative region, while the positive region shrinks and weakens. By integrating the spin Berry curvature in the Brillouin zone a large magnitude of the negative ISHC is obtained for AA stacking, with a value of -30.22 $(\hbar/e)$ (S/cm).

To further analyze the influence of stacking modes on ISHC, we plot band-decomposed charge densities as shown in Fig. 3. Since VB4 and VB5 reverse their contributions to the spin Berry curvature when the stacking mode changes, we mainly focus on these valence bands. For the AA stacking configuration, the interlayer distance is only 2.39 Å, which is significantly smaller than that in MoS_2 and other TMDs bilayers [51]. As a result, a large binding energy and strong interlayer interaction are expected. As shown in Figs. S4 and S6 in the Supplemental Material [49], both VB4 and VB5 are mainly composed of in-plane p_x and p_y states of Te atoms. Due to the short interlayer distance and strong interlayer interaction, these states in upper and lower layers are strongly hybridized. This can be further confirmed by the interlayer differential charge densities, which are obtained by subtracting the charge density of the $PtTe_2$ bilayer from that of the independent top and bottom $PtTe_2$ monolayers. As shown in Fig. 3(c), sufficient electrons are localized in the interlayer region. Such electronic interlayer hybridization is no longer a simple vdW interaction, but rather a "covalentlike quasibonding." In this sense, each Te atom can be regarded as bonded by a spring in a tilted octahedral configuration as illustrated in Fig. 3(c).

In terms of the AB stacking configuration, however, the interlayer distance reaches to 2.87 Å. In addition, the binding energy is 0.21 eV higher as compared with that in the AA stacking mode. Accordingly, the interlayer interaction in AB weakens. In Fig. 3(b), one can clearly see that the interlayer hybridization vanishes. A negligible charge is distributed in the interlayer region, showing a vdW characteristic [see Fig. 3(d)]. In order to understand the charge-spin conversion manipulated by stacking mode, we also calculate the spin textures of the AA and AB stacking configurations. As shown clearly in Figs. 3(e) and 3(f), the helical spin texture precesses in opposite directions for the AA and AB stacking modes, especially around the Γ and K points, which is consistent with the ISHC calculations.

Based on the above results, we can conclude that tuning the stacking mode is an effective way to manipulate the ISHC in bilayer $PtTe_2$. In view of this, we calculate the ISHC for the full 2D space by performing a lateral shift of the top $PtTe_2$ layer parallel to the bottom $PtTe_2$ layer, in which a total of 144 different stacking configurations are calculated. The results are then interpolated via the spline function as illustrated in Fig. 4 (the original results are shown in Fig. S8 in the Supplemental Material [49]). We find that during the whole process of lateral shift, AA stacking is the most stable order, which has the strongest binding energy as well as the shortest interlayer distance. As a result, a strong interlayer coupling is expected, which gives rise to covalentlike bonding as has been discussed above. These strong hybridized bonds give rise to a negative value of the ISHC. The interlayer distance becomes larger if we shift the top $PtTe_2$ layer from the AA stacking mode along the [100] direction (see Fig. S2 in the Supplemental Material [49]). The interlayer binding energy also weakens at the same time. Consequently, a vdW interaction within the interlayer region is expected. The contributions of energy bands near the Fermi level to the spin Berry curvature reverse their signs, leading to positive ISHC. If the stacking mode of the $PtTe_2$ bilayer changes to AB′ stacking order, the interlayer distance is considerably larger. In this case, the interlayer interaction is extremely weak. As a result, the top and bottom layers have little interlayer coupling, and the $PtTe_2$ bilayer shows semiconducting monolayer characteristics, sharing similar behavior of the ISHC with its monolayer counterpart (see Figs. S9 and S10 in the Supplemental Material [49]).

IV. CONCLUSIONS

In summary, we show that the sign of the ISHC can be reversed upon stacking transitions in bilayer $PtTe_2$. As such, stacking order is an efficient way to control and manipulate the spin current through the SHE. Further analysis reveals that such reversion can be ascribed to the interlayer coupling. If the interlayer coupling is weak, for example, in the AB′ stacking mode, vdW interaction is expected within the interlayer region. In this case, the band structure as well as the ISHC for the bilayer system is comparable or shares

similar behavior with its monolayer counterpart. By contrast, if the interlayer coupling is strong, e.g., in the AA stacking mode, large interlayer electronic hybridization occurs. The high localized charges within the interlayer region result in covalentlike quasibonding, which may significantly tailor the spin Berry curvature along with the ISHC. In this sense, one can effectively tune the ISHC through stacking transitions in 2D bilayer or multilayer materials, especially for those with strong interlayer interactions. The results presented in this paper not only elucidate an important fundamental insight into the nature of stacking-dependent ISHC in 2D TMDs but also pave the way for design of next-generation ultrathin and flexible spintronic devices.

ACKNOWLEDGMENTS

The authors are thankful for fruitful discussions with Prof. Zhirui Gong. The authors also acknowledge the support from the Natural Science Foundation of Guangdong Province (Grant No. 2019A1515010750) and the Natural Science Foundation of Shenzhen (Grant No. JCYJ20190808152801642).

[1] S. Murakami, N. Nagaosa, and S.-C. Zhang, Science **301**, 1348 (2003).
[2] Y. K. Kato, R. C. Myers, A. C. Gossard, and D. D. Awschalom, Science **306**, 1910 (2004).
[3] J. Sinova, D. Culcer, Q. Niu, N. A. Sinitsyn, T. Jungwirth, and A. H. MacDonald, Phys. Rev. Lett. **92**, 126603 (2004).
[4] M. Z. Hasan and C. L. Kane, Rev. Mod. Phys. **82**, 3045 (2010).
[5] J. Sinova, S. O. Valenzuela, J. Wunderlich, C. H. Back, and T. Jungwirth, Rev. Mod. Phys. **87**, 1213 (2015).
[6] N. Nagaosa, J. Sinova, S. Onoda, A. H. MacDonald, and N. P. Ong, Rev. Mod. Phys. **82**, 1539 (2010).
[7] M. Dyakonov and V. Perel, Phys. Lett. A **35**, 459 (1971).
[8] J. E. Hirsch, Phys. Rev. Lett. **83**, 1834 (1999).
[9] S. Zhang, Phys. Rev. Lett. **85**, 393 (2000).
[10] H. Kontani, T. Tanaka, D. S. Hirashima, K. Yamada, and J. Inoue, Phys. Rev. Lett. **100**, 096601 (2008).
[11] G. Y. Guo, S. Murakami, T.-W. Chen, and N. Nagaosa, Phys. Rev. Lett. **100**, 096401 (2008).
[12] M. Gradhand, D. V. Fedorov, P. Zahn, and I. Mertig, Phys. Rev. B **81**, 245109 (2010).
[13] N. H. Long, P. Mavropoulos, B. Zimmermann, D. S. G. Bauer, S. Blügel, and Y. Mokrousov, Phys. Rev. B **90**, 064406 (2014).
[14] B. Zimmermann, K. Chadova, D. Ködderitzsch, S. Blügel, H. Ebert, D. V. Fedorov, N. H. Long, P. Mavropoulos, I. Mertig, Y. Mokrousov, and M. Gradhand, Phys. Rev. B **90**, 220403(R) (2014).
[15] H.-A. Engel, B. I. Halperin, and E. I. Rashba, Phys. Rev. Lett. **95**, 166605 (2005).
[16] T. Funato and H. Kohno, Phys. Rev. B **102**, 094426 (2020).
[17] T. Jungwirth, Q. Niu, and A. H. MacDonald, Phys. Rev. Lett. **88**, 207208 (2002).
[18] T. Tanaka, H. Kontani, M. Naito, T. Naito, D. S. Hirashima, K. Yamada, and J. Inoue, Phys. Rev. B **77**, 165117 (2008).
[19] V. T. Pham, L. Vila, G. Zahnd, A. Marty, W. Savero-Torres, M. Jamet, and J.-P. Attane, Nano Lett. **16**, 6755 (2016).
[20] F. Freimuth, S. Blügel, and Y. Mokrousov, Phys. Rev. Lett. **105**, 246602 (2010).
[21] X. Sui, C. Wang, J. Kim, J. Wang, S. H. Rhim, W. Duan, and N. Kioussis, Phys. Rev. B **96**, 241105(R) (2017).
[22] X. Qian, J. Liu, L. Fu, and J. Li, Science **346**, 1344 (2014).
[23] C. K. Safeer, J. Ingla-Aynés, N. Ontoso, F. Herling, W. Yan, L. E. Hueso, and F. Casanova, Nano Lett. **20**, 4573 (2020).
[24] X. Chia, A. Adriano, P. Lazar, Z. Sofer, J. Luxa, and M. Pumera, Adv. Funct. Mater. **26**, 4306 (2016).
[25] W. Yao, E. Wang, H. Huang, K. Dent, M. Yan, K. Zhang, K. Miyamoto, T. Okuda, L. Li, Y. Wang, H. Gao, C. Liu, W. Duan, and S. Zhou, Nat. Commun. **8**, 14216 (2017).
[26] M.-K. Lin, R. A. B. Villaos, J. A. Hlevyack, P. Chen, R.-Y. Liu, C.-H. Hsu, J. Avila, S.-K. Mo, F.-C. Chuang, and T.-C. Chiang, Phys. Rev. Lett. **124**, 036402 (2020).
[27] T. Chowdhury, E. C. Sadler, and T. J. Kempa, Chem. Rev. (Washington, DC) **120**, 12563 (2020).
[28] W. Feng, Y. Yao, W. Zhu, J. Zhou, W. Yao, and D. Xiao, Phys. Rev. B **86**, 165108 (2012).
[29] L. Matthes, S. Küfner, J. Furthmüller, and F. Bechstedt, Phys. Rev. B **94**, 085410 (2016).
[30] J. Sławińska, F. T. Cerasoli, H. Wang, S. Postorino, A. Supka, S. Curtarolo, M. Fornari, and M. B. Nardelli, 2D Mater. **6**, 025012 (2019).
[31] X. Liu, A. P. Pyatakov, and W. Ren, Phys. Rev. Lett. **125**, 247601 (2020).
[32] J. Xiao, Y. Wang, H. Wang, C. D. Pemmaraju, and A. M. Lindenberg, Nat. Phys. **16**, 1 (2020).
[33] Y. Zhao, J. Qiao, P. Yu, Z. Hu, Z. Lin, S. P. Lau, Z. Liu, W. Ji, and Y. Chai, Adv. Mater. (Weinheim) **28**, 2399 (2016).
[34] K. Deng, M. Yan, C.-P. Yu, J. Li, X. Zhou, K. Zhang, Y. Zhao, K. Miyamoto, T. Okuda, W. Duan, Y. Wu, X. Zhong, and S. Zhou, Sci. Bull. **64**, 1044 (2019).
[35] S. Hao, J. Zeng, T. Xu, X. Cong, C. Wang, C. Wu, Y. Wang, X. Liu, T. Cao, G. Su, L. Jia, Z. Wu, Q. Lin, L. Zhang, S. Yan, M. Guo, Z. Wang, P. Tan, L. Sun, Z. Ni *et al.*, Adv. Funct. Mater. **28**, 1803746 (2018).
[36] H. Xu, J. Wei, H. Zhou, J. Feng, T. Xu, H. Du, C. He, Y. Huang, J. Zhang, Y. Liu, H.-C. Wu, C. Guo, X. Wang, Y. Guang, H. Wei, Y. Peng, W. Jiang, G. Yu, and X. Han, Adv. Mater. (Weinheim) **32**, 2000513 (2020).
[37] P. Giannozzi, O. Andreussi, T. Brumme, O. Bunau, M. B. Nardelli, M. Calandra, R. Car, C. Cavazzoni, D. Ceresoli, M. Cococcioni, N. Colonna, I. Carnimeo, A. D. Corso, S. de Gironcoli, P. Delugas, R. A. DiStasio, A. Ferretti, A. Floris, G. Fratesi, G. Fugallo *et al.*, J. Phys.: Condens. Matter **29**, 465901 (2017).
[38] P. Giannozzi, O. Baseggio, P. Bonfà, D. Brunato, R. Car, I. Carnimeo, C. Cavazzoni, S. de Gironcoli, P. Delugas, F. Ferrari Ruffino, A. Ferretti, N. Marzari, I. Timrov, A. Urru, and S. Baroni, J. Chem. Phys. **152**, 154105 (2020).
[39] J. P. Perdew, K. Burke, and M. Ernzerhof, Phys. Rev. Lett. **77**, 3865 (1996).

[40] S. Grimme, J. Antony, S. Ehrlich, and H. Krieg, J. Chem. Phys. **132**, 154104 (2010).
[41] N. Marzari and D. Vanderbilt, Phys. Rev. B **56**, 12847 (1997).
[42] G. Pizzi, V. Vitale, R. Arita, S. Bluegel, F. Freimuth, G. Geranton, M. Gibertini, D. Gresch, C. Johnson, T. Koretsune, J. Ibanez-Azpiroz, H. Lee, J.-M. Lihm, D. Marchand, A. Marrazzo, Y. Mokrousov, J. I. Mustafa, Y. Nohara, Y. Nomura, L. Paulatto *et al.*, J. Phys.: Condens. Matter **32**, 165902 (2020).
[43] J. Qiao, J. Zhou, Z. Yuan, and W. Zhao, Phys. Rev. B **98**, 214402 (2018).
[44] Y. G. Yao, L. Kleinman, A. H. MacDonald, J. Sinova, T. Jungwirth, D. S. Wang, E. G. Wang, and Q. Niu, Phys. Rev. Lett. **92**, 037204 (2004).
[45] J. Shi, P. Zhang, D. Xiao, and Q. Niu, Phys. Rev. Lett. **96**, 076604 (2006).
[46] C. Xiao and Q. Niu, arXiv:2009.12058.
[47] D. Monaco and L. Ulčakar, Phys. Rev. B **102**, 125138 (2020).
[48] Y. Zhao, Y. Hu, L. Liu, Y. Zhu, and H. Guo, Nano Lett. **11**, 2088 (2011).
[49] See Supplemental Material at http://link.aps.org/supplemental/10.1103/PhysRevB.103.125403 for the geometric structures, projected band structures, and spin Berry curvature along high-symmetry points of the Brillouin zone for different stacking configurations.
[50] J. Zhou, J. Qiao, A. Bournel, and W. Zhao, Phys. Rev. B **99**, 060408(R) (2019).
[51] C. Long, Y. Dai, Z.-R. Gong, and H. Jin, Phys. Rev. B **99**, 115316 (2019).